Research Article | Vol. 34, No. 7 / July 2017 / Journal of the Optical Society of America B 1465

Journal of the Optical Society of America B

OPTICAL PHYSICS

Single-slot hybrid microring resonator hydrogen sensor

KENAN CICEK,[1,2,4,*] MUSTAFA ERYÜREK,[2] AND ALPER KIRAZ[2,3]

[1]Department of Electrical and Electronics Engineering, Iğdr University, Iğdr, Turkey
[2]Department of Physics, Koç University, Rumelifeneri Yolu, 34450 Saryer, İstanbul, Turkey
[3]Department of Electrical and Electronics Engineering, Koç University, Rumelifeneri Yolu, 34450 Saryer, İstanbul, Turkey
[4]Department of Electrical and Electronics Engineering, Merchant Venturers School of Engineering, University of Bristol, Bristol, UK
*Corresponding author: eexkc@my.bristol.ac.uk

Received 29 March 2017; revised 13 May 2017; accepted 24 May 2017; posted 31 May 2017 (Doc. ID 291699); published 20 June 2017

Photonic integrated circuits fabricated on silicon-on-insulator platforms offer convenient foundations to implement highly sensitive, compact, robust, and low-cost technology in sensing applications. The potential of this technology in hydrogen gas sensing is discussed in this study. A single-slot hybrid microring-resonator- (MRR) based hydrogen gas sensor utilizing a coaxial palladium (Pd) microdisk is demonstrated. Detection is based on expansion of Pd upon hydrogen exposure toward the slot between the outer radius of the Pd microdisk and the inner radius of the MRR and the subsequent shift of the whispering gallery modes (WGMs) propagating in the MRR. Finite-difference time-domain simulations indicate a sensitivity as high as 11.038 nm/% hydrogen, provided that optimum geometrical design parameters are chosen. This sensitivity value is ~23 times higher than other existing WGM-based hydrogen sensor demonstrations.

OCIS codes: (230.5750) Resonators; (130.6010) Sensors; (130.3120) Integrated optics devices; (130.3990) Micro-optical devices.

https://doi.org/10.1364/JOSAB.34.001465

1. INTRODUCTION

Hydrogen is a highly flammable gas which has been studied with great interest [1] for a long time, especially due to its potential as an environmentally friendly fuel [2]. At room temperature, hydrogen has lower and upper explosive limits of 4% and 75% in air [3], respectively. These values reveal the largest flammability range as compared to other explosive gasses, such as propane, natural gas, and methane gasoline. Hydrogen gas holds a higher risk of leaking not only because the hydrogen molecule is the smallest molecule but also because hydrogen is the lightest element in the periodic table. Due to its wide flammability range and great leaking tendency, monitoring of hydrogen gas with a high sensitivity is a critical challenge.

Numerous hydrogen gas detection methods have been presented employing different mechanisms based on thermal [4], electrical [5], mechanical [6], acoustic [7], or optical [8] responses. As compared to other methods, optical sensor devices promise to yield highly sensitive, relatively compact, low-cost, and reliable operation. To date, various different optical detection schemes benefiting from surface plasmon resonances [9,10], photonic crystals [11], Bragg gratings [12–14], optical fibers [15], and optical microresonators [16] have been demonstrated.

Hydrogen sensors that use optical microresonators have great potential to possess very high sensitivities because of the high quality factors (Q-factors) of their optical resonances [17]. In a recent study [16], a hybrid structure of polymer microdisk microresonator coated with a coaxial thin palladium (Pd) layer, a highly favorable element for hydrogen detection [18–20], is presented with detection sensitivities down to 0.3%. The sensing mechanism in this study relies on the volumetric expansion of the Pd layer in the presence of hydrogen gas that results in the size change of the polymer microdisk. Such size changes are very sensitively measured using the spectral position of the optical resonances called whispering gallery modes (WGMs). Another past study proposed to employ a single-slot hybrid plasmonic structure made of a microring resonator (MRR) fabricated using silicon-on-insulator (SOI) technology and a coaxial Au disk for highly sensitive label-free optical detection [21]. This study utilizes the plasmonic technology to trap the optical energy in a narrow slot in the upper cladding, which gives rise to a large overlap between the WGM and the sensing medium. Hence, any small change in the sensing medium results in a relatively large shift in WGM resonant wavelengths leading to highly sensitive detection of the cladding refractive index. For hybrid structures, sensitivities up to 580 nm/RIU are predicted as compared to 75 nm/RIU for the case when a nonhybrid single-slot structure is employed [22]. When a double-slot hybrid ring resonator is used, however, the sensitivity increases even more up to 687.5 nm/RIU [23]

In this study, we combine the ideas presented in Ref. [21] with Ref. [16] and demonstrate that the structure employed in

Ref. [21] enables highly sensitive hydrogen gas detection when the inner coaxial disk made of Au is replaced by a Pd coaxial disk. The sensing mechanism relies on the expansion of Pd and subsequent spectral shifts of the WGMs propagating in the MRR. The expansion in the Pd disk as a result of the hydrogen gas adsorption shrinks the slot where the optical power is trapped. This leads to an increase in the effective refractive index of the medium surrounding the MRR, resulting in the redshift of the WGM spectral positions. In order to quantify the potential of the proposed method in hydrogen sensing, finite-difference time-domain (FDTD) simulations are performed and the sensing performances observed for different geometrical design parameters are compared.

2. SENSOR STRUCTURE

Figure 1 shows the schematic diagram of the proposed single-slot hybrid sensor for hydrogen sensing. The sensor comprises an MRR with inner radius R_{in} and outer radius R_{out} (the width of the MRR is $W_{MRR} = R_{out} - R_{in}$) designed on SOI technology. The MRR is coupled to a pair of access waveguides, which have 400 nm width and 220 nm height (for experimental studies). A coaxial Pd disk with radius R_{Pd} is placed inside the MRR. Metals such as Pd have both Drude and Lorentz components for the dielectric function. Thus, Lorentz–Drude expressions are followed to define the optical properties of Pd [24]. The optical parameters for Pd used in our calculations are provided in Ref. [24] for a large frequency range. In our calculations, the refractive indices of air and silicon MRRs are used as 1.000293 and 3.476, respectively. The slot between the inner edge of the MRR and the Pd disk has a width of $w_{slot} = R_{in} - R_{Pd}$. A TE-polarized incident beam with Gaussian spectrum is injected into the MRR through the input port as represented in Fig. 1(a). Excited WGM within the resonator interacts with upper cladding via an evanescent tail and couple out from the MRR through the drop port of the MRR.

The spectrum from the drop port is tracked for monitoring the change in resonant wavelength. In order to guide future experimental studies, the Pd disk is assumed to be in contact with the substrate only at its center, as shown in Fig. 1(b), to avoid tension and strain that may occur after the expansion and to allow unrestrained expansion. In addition, the Pd disk can also have a few holes around the center, as depicted in Fig. 1, so that the etching of the silica layer beneath the Pd disk can be possible [25].

The FDTD method is used to simulate the proposed four-port MRR structure in an attempt to study its hydrogen sensing potential. The numerical calculations are performed in 2D due to the limitation of the sources. Even though the actual proposed device has a 3D geometry, 2D calculations give sufficient insight about the performance of the structure with approximate numerical results as 3D [26]. A fine grid size as small as 2 nm and sufficient operation time is used for high accuracy and reliability of the simulations. For the calculations, the Si MRR and coupled waveguide system is assumed to be placed in an air-sensing medium.

Field distributions of a TE-polarized light beam in 500 nm, 400 nm, and 300 nm wide waveguides are shown in Figs. 2(a), 2(b), and 2(c), respectively. As seen in these figures, a portion of the light is guided by a 500 nm waveguide with an evanescent field, which fades away within a short distance. In comparison, as the waveguide gets narrower, it results in a weaker confinement of the guided modes, which stretch symmetrically mostly in the horizontal direction [27]. Thus, the evanescent field expands further outside the waveguide interacting more with the cladding ambient, as shown in Figs. 2(b) and 2(c).

In the case of hydrogen sensing, when the Pd disk is exposed to hydrogen, it undergoes an expansion due to the formation of palladium hydride [28] and gets closer to the inner edge of the resonator as the concentration of hydrogen in the ambient, C_{hyd}, increases. This way, the evanescent field is pushed toward the silicon core, causing the effective refractive index of the surrounding medium to increase [21]. This change in effective refractive index causes a redshift in WGMs, which is the

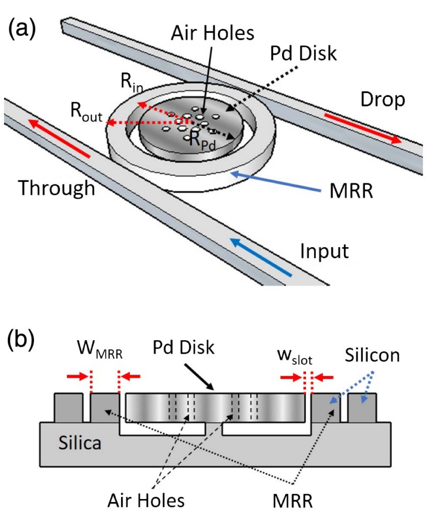

Fig. 1. (a) Schematic architecture of the proposed hydrogen sensing device and (b) its cross-sectional view.

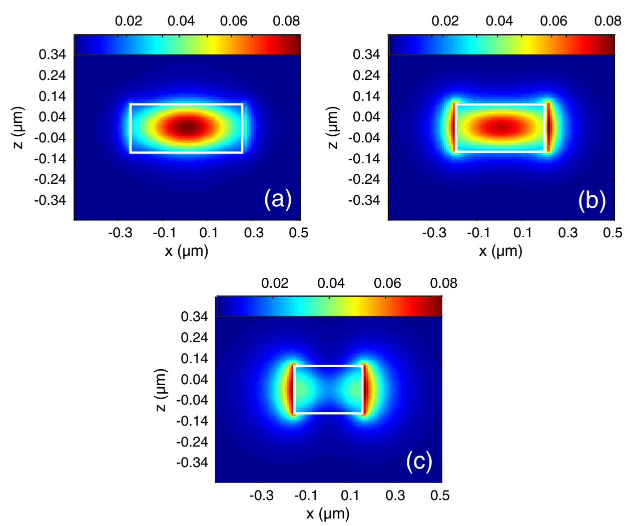

Fig. 2. Electric field (E-field) distribution at the cross section of the (a) $W_{MRR} = 500$ nm, (b) $W_{MRR} = 400$ nm, and (c) $W_{MRR} = 300$ nm waveguide at the wavelengths of 1523 nm, 1517 nm, and 1512 nm, respectively. As the waveguide width decreases, the evanescent field stretches further away from the waveguide into the ambient.

deterministic character in the presented system. In this work, only 300 nm and 400 nm wide MRR waveguides are numerically studied to show the effect of MRR width on sensing.

3. RESULTS AND DISCUSSION

It is known that the Pd lattice exhibits a lattice expansion by 0.087% in the presence of 1% hydrogen gas (H_2) in the environment [29]. For H_2 concentrations between 0% and 1%, the expansion is reversible, i.e., alpha phase. Based on this information, various sensor geometries employing MRRs with different radii and width values are numerically simulated. Three different sizes of Pd disk are used for each sensor geometry. Each hydrogen sensor is studied for C_{hyd} ranging between 0% and 1%.

The simulations are performed by increasing the Pd disk size by 5 nm at each calculation loop due to limitations caused by the selected fine grid size of 2 nm. Simulated $\Delta\lambda$ values are then interpolated with nonlinear curve fitting to estimate sensitivities at much lower hydrogen concentration levels. As an example,

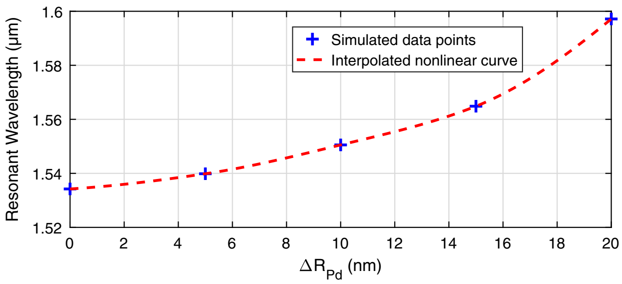

Fig. 3. Interpolation of simulated data for a geometry where $R_{\mathrm{out}} = 1$ µm, $W_{\mathrm{MRR}} = 300$ nm, and $w_{\mathrm{slot}} = 30$ nm. For these geometry values, $\Delta R_{\mathrm{Pd}} = 5$ nm corresponds to $C_{\mathrm{hyd}} = 8.57\%$, assuming linear expansion of the lattice constant of Pd with H_2.

interpolation of a data set obtained from the geometry where $R_{\mathrm{out}} = 1$ µm, $W_{\mathrm{MRR}} = 300$ nm, and $w_{\mathrm{slot}} = 30$ nm is shown in Fig. 3. The resonant wavelength of the mode under test (ninth mode, shown in Fig. 4) is observed after each increment in ΔR_{Pd}. C_{hyd} values corresponding to the specific ΔR_{Pd} values are calculated considering the lattice expansion of Pd in the presence of H_2 (0.087% lattice expansion for 1% H_2 [29]). A nonlinear curve is then fitted to the resulting $\Delta\lambda$; C_{hyd} points and this curve are used for interpolating the dependence of $\Delta\lambda$ on C_{hyd} for all intermediate values. Throughout this paper, this procedure is followed to study the change of $\Delta\lambda$ within the C_{hyd} range of 0%–1%.

Figure 5 shows the relation between wavelength shift ($\Delta\lambda$) and C_{hyd} based on w_{slot} for MRRs with three different values of R_{out} (1.00 µm, 2.00 µm, and 3.00 µm) and two different W_{MRR} (300 nm and 400 nm) values. In Figs. 5(a) and 5(b), the results from 300 nm to 400 nm wide MRRs, respectively, are demonstrated for $R_{\mathrm{out}} = 1.00$ µm. As can be seen from both graphs, $\Delta\lambda$ in response to C_{hyd} gradually increases along with the concentration increment. The wavelength shift, whose rate of increase depends on w_{slot}, reaches values as high as 1500 pm for $C_{\mathrm{hyd}} = 1\%$ with a 300 nm wide MRR. However, for a 400 nm wide MRR, this value remains much smaller at around 150 pm.

Figures 5(c) and 5(d) show the dependence of $\Delta\lambda$ on C_{hyd} for 300 nm and 400 nm wide MRRs, respectively, with an outer radii of $R_{\mathrm{out}} = 2.0$ µm. These figures show that the sensitivity of $\Delta\lambda$ on C_{hyd} can be further increased by employing larger MRR structures. As presented in Fig. 5(c), a wavelength shift around 6000 pm is observed for $C_{\mathrm{hyd}} = 1\%$ from 300 nm wide MRR with $R_{\mathrm{out}} = 2.00$ µm. For constant w_{slot} and W_{MRR} values, $\Delta\lambda$ increases as R_{out} increases due to the increase of interaction length between Pd and MRR structures. This is shown in Figs. 5(b) and 5(d). In these figures for a given W_{MRR} value of 400 nm, $\Delta\lambda$ calculated for $C_{\mathrm{hyd}} = 1\%$ reduces from 1502 pm to 159 pm when R_{out} is changed from 2.00 µm to

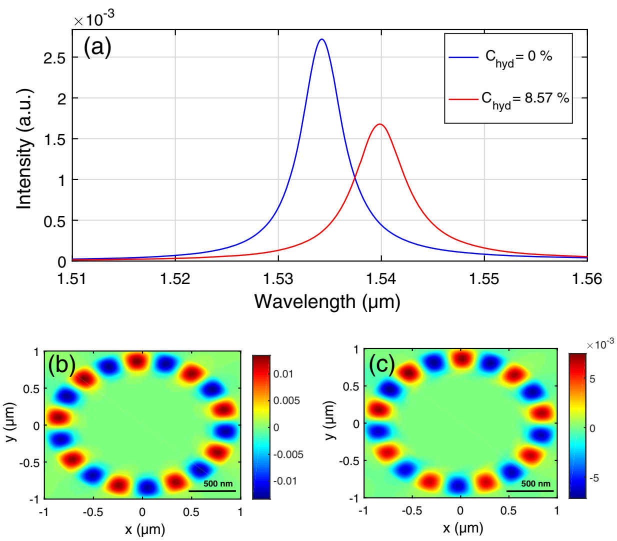

Fig. 4. (a) Spectra observed at the drop port of an MRR sensor with $R_{\mathrm{out}} = 1.0$ µm, $W_{\mathrm{MRR}} = 300$ nm, and $w_{\mathrm{slot}} = 30$ nm when $C_{\mathrm{hyd}} =$ 0% and 8.57%. H_z field patterns of MRRs with $w_{\mathrm{slot}} = 30$ nm in (b) 0% and (c) 8.57% C_{hyd} ambient.

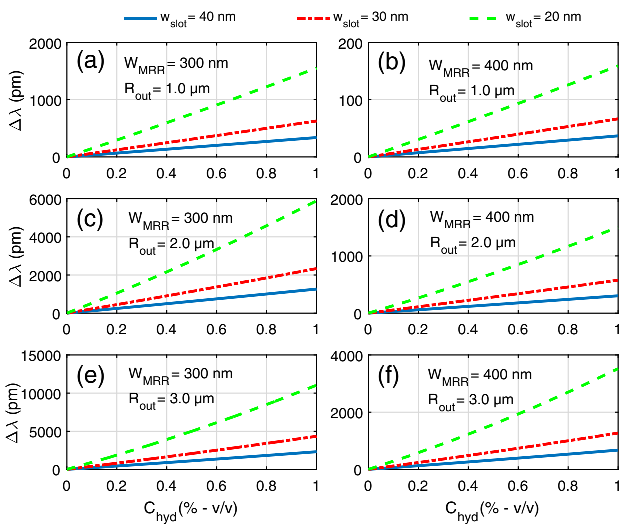

Fig. 5. Spectral shifts observed from MRR sensors with (a, c, e) $W_{\mathrm{MRR}} = 300$ nm and (b, d, f) 400 nm for (a, b) $R_{\mathrm{out}} =$ 1.00 µm, (c, d) 2.00 µm, and (e, f) 3.00 µm as a function of hydrogen concentration for various w_{slot} values.

1.00 μm. Moreover, for $R_{out} = 3.00$ μm and $C_{hyd} = 1\%$, $\Delta\lambda$ reaches 11038 pm and 3520 pm for $W_{MRR} = 300$ nm and $W_{MRR} = 400$ nm, respectively, as shown in Figs. 5(e) and 5(f). Hence, reducing W_{MRR} increases the sensitivity of the presented hydrogen sensor. $\Delta\lambda$ also varies with regard to w_{slot}. As can be seen from Fig. 5, it is clear that when constant W_{MRR} and R_{out} values are considered, decreasing w_{slot} results in larger $\Delta\lambda$, i.e., increased sensitivity.

Exemplary WGM spectra observed from the drop port for $W_{MRR} = 300$ nm, $R_{out} = 1.0$ μm, and $w_{slot} = 30$ nm for 0% and 8.57% C_{hyd} are plotted in Fig. 4(a). The WGM shift is of the order of nanometers [see Fig. 5(a)]. These large shifts in WGM resonances are highly desirable for the sensitive detection of hydrogen. However, if the shift is too much, then it may result in a change in the mode number of the WGM, which compromises the reliability of the detection. To make sure the mode number does not change between 0% and 1% C_{hyd}, the magnetic field intensity distribution of the WGM in the z-direction, H_z, is plotted in Figs. 4(b) and 4(c) for 0% and 8.57% C_{hyd}, respectively. The results reveal that the WGMs under study have the same azimuthal mode number of 9. This indicates the reliability of sensing throughout the change in C_{hyd}.

Up to this point, $\Delta\lambda$ is considered only due to the expansion of Pd. However, the refractive index of Pd also changes under changing C_{hyd} because of the formation of palladium hydride. $\Delta\lambda$ can be defined as $\Delta\lambda = \Delta\lambda_{exp} + \Delta\lambda_{ref}$, where $\Delta\lambda_{exp}$ and $\Delta\lambda_{ref}$ are the WGM shifts due to the expansion of Pd and the refractive index change of Pd, respectively. In order to ensure that $\Delta\lambda_{exp}$ is dominant over $\Delta\lambda_{ref}$, a control simulation is performed. A structure with $W_{MRR} = 300$ nm, $w_{slot} = 40$ nm, and $R_{out} = 2.0$ μm is simulated with changing the refractive index of Pd based on Ref. [30] without changing the radius of the Pd microdisk. From the simulation results where C_{hyd} is changed from 0% to 1%, it is found that $\Delta\lambda_{ref} = 75.9$ pm, whereas $\Delta\lambda_{exp} = 1.5$ nm [see Fig. 5(c)]. Therefore, it is concluded that $\Delta\lambda_{exp}$ is considered to be dominant over $\Delta\lambda_{ref}$ and $\Delta\lambda_{ref}$ is completely disregarded in our calculations.

In order to measure the wavelength shift in response to the Pd radius change, the sensitivity (S) of the sensor is calculated using $S = \Delta\lambda_{res}/\Delta C_{hyd}$, where λ_{res} is the resonant wavelength of a WGM. FDTD simulation results shown in Fig. 5 reveal that as w_{slot} or W_{MRR} decreases, S increases. These results are summarized Figs. 6(a) and 6(b), where S is plotted as a function of w_{slot} for different R_{out} and W_{MRR} values. S itself is not enough to describe the sensing capability of the MRR sensor. Q-factors of the WGMs should also be considered. The Q-factor of each geometry is calculated for $C_{hyd} = 0\%$ and depicted in Figs. 6(c) and 6(d). In Fig. 6(c), for $W_{MRR} = 300$ nm, the Q-factor is observed to increase with w_{slot} because as the w_{slot} increases, the overlap between WGM and Pd decreases, which eventually decreases the absorption losses. In addition, in Fig. 6(c), the Q-factor is larger for smaller R_{out} because the total interaction length of the Pd disk with optical power is smaller, implying lower absorption. However, the dependencies of the Q-factor on w_{slot} shown in Fig. 6(d) are different than those shown Fig. 6(c). In this case, for $W_{MRR} = 400$ nm, WGMs propagate more in the core of the MRR, making bending losses

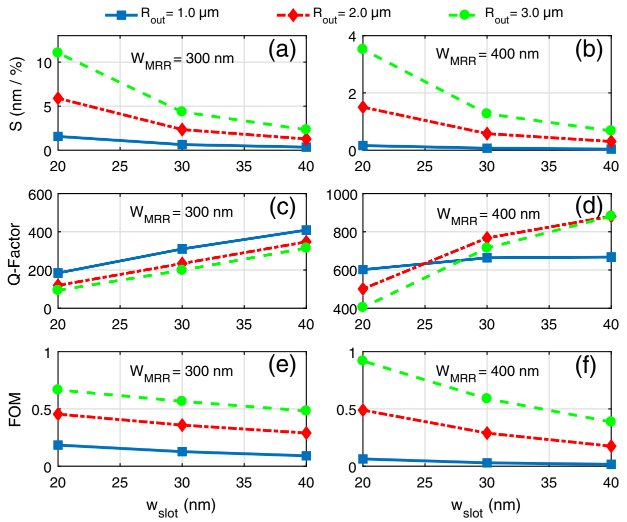

Fig. 6. (a, b) Sensitivity, (c, d) Q-factor, and (e, f) FOM changes as a function of w_{slot} for various R_{out} values with (a, c, e) $W_{MRR} = 300$ nm and (b, d, f) $W_{MRR} = 400$ nm.

dominant over the absorption losses. For $w_{slot} = 20$ nm, absorption losses are dominant. Hence, the MRR with the smallest radius of 1.0 μm has the highest Q-factor. In contrast, for $w_{slot} = 40$ nm, bending losses start to become dominant and the MRR with the smallest radius attains the lowest Q-factor. The results presented in Figs. 6(a)–6(d) show a trade-off between the sensitivity and the Q-factor. For a fair evaluation of the sensor performance based on the geometrical differences, a figure of merit (FOM) is defined as $\mathrm{FOM} = SQ/\lambda_{res}$, where Q indicates the Q-factor [21]. FOM values of different sensor geometries are shown in Figs. 6(e) and 6(f). A maximum FOM of 0.92 is achieved for a sensor with $W_{MRR} = 400$ nm, $R_{out} = 3.0$ μm, and $w_{slot} = 20$ nm. Even though this specific geometry has the highest performance, in general, MRRs with $R_{out} = 3.0$ μm and $W_{MRR} = 300$ nm or 400 nm are observed to show good performance that reveals FOM values higher than 0.4 when w_{slot} is selected between 20 and 40 nm [Figs. 6(e) and 6(f)]. FOM values are calculated as 0.02 [16], 0.4 [31], and 7.8 [17] for the previous microresonator-based hydrogen sensor demonstrations in the literature. Hence, when FOM values are considered, our proposed sensor performs better than [16] and [31] but worse than [17]. However, in Ref. [17], Pd is not employed and hydrogen sensing is achieved by

Table 1. Comparison of Sensitivity (S) and Figure of Merit (FOM) Values between the Demonstrated Single-Slot Hybrid MRR Hydrogen Sensor and Other Microresonator-Based Hydrogen Sensors from the Literature

References	[16]	[17]	[28]	Single-Slot Hybrid MRR
S (pm/%)	32	480	20	11038
FOM	0.02	7.8	0.4	0.92
Reversibility	√	×	√	√

catalytic combustion, which an irreversible process. In terms of sensitivity, however, the proposed sensor with geometrical parameters of $R_{out} = 3.0$ μm, $w_{slot} = 20$ nm, and $W_{MRR} = 300$ nm provides a maximum sensitivity of 11.038 nm/% hydrogen, which is much larger than the sensitivities of ~20 pm/% [31], 32 pm/% [16], and 480 pm/% [17] reported in previous microresonator-based hydrogen sensor demonstrations (see Table 1).

4. CONCLUSION

In this work, a novel geometry for hydrogen sensing with single-slot hybrid microring resonators is demonstrated and verified by FDTD simulations. The geometry employs a Pd microdisk placed coaxially inside an SOI-based Si MRR with a small gap in between ($w_{slot} = 20$–40 nm). WGMs of the MRR exhibit redshifts in their spectra due to the expansion of the Pd microdisk with increasing hydrogen concentration in the ambient. Such a red spectral shift can also be observed due to pure refractive index change of Pd upon hydrogen exposure; however, our calculations show that for our parameter values, the observed spectral shifts are mainly caused by the volumetric expansion of the Pd microdisk rather than a pure refractive index change. The sensitivity of the device increases as w_{slot} decreases, W_{MRR} decreases, or R_{out} increases. With an optimal design, detection sensitivity of 11.038 nm/% hydrogen can be achieved, which is more than ~23 times more sensitive than previous optical microresonator-based hydrogen sensor demonstrations [16,17,31]. However, there is a trade-off between the Q-factor and the sensitivity observed for a WGM. A figure of merit is defined and it is determined that within the parameter space that is explored, the best sensor performance is observed for $R_{out} = 3.0$ μm, $W_{MRR} = 300$ nm or 400 nm, and $w_{slot} = 20$–40 nm. For these sensor parameters, figure of merit values between 0.4 and 1 are calculated. These values correspond to a 2.5–50 fold enhancement over the previous experimental demonstrations shown in Refs. [16, 31]. Although the sensor presented in Ref. [17] exhibits an FOM of 7.8, its lack of reversibility due to the underlying sensing mechanism that relies on catalytic combustion yields a severe disadvantage as compared to our study. The calculated FOM values do not represent a fundamental limit for the sensor demonstrated in this study. Our preliminary calculations for $R_{out} = 5.0$ μm and $w_{slot} = 20$ nm revealed an FOM value of 4.57. Thus, there is high potential in further improving the performance (Q-factor, sensitivity, and FOM) of the presented single-slot hybrid MRR sensor by changing the geometrical sensor parameters.

REFERENCES

1. C. Christofides and A. Mandelis, "Solid-state sensors for trace hydrogen gas detection," J. Appl. Phys. **68**, R1–R30 (1990).
2. T. Hübert, L. Boon-Brett, G. Black, and U. Banach, "Hydrogen sensors—a review," Sens. Actuators B **157**, 329–352 (2011).
3. H. Gu, Z. Wang, and Y. Hu, "Hydrogen gas sensors based on semiconductor oxide nanostructures," Sensors **12**, 5517–5550 (2012).
4. E.-B. Lee, I.-S. Swang, J.-H. Cha, H.-J. Lee, W.-B. Lee, J. J. Pak, J.-H. Lee, and B.-K. Ju, "Micromachined catalytic combustible hydrogen gas sensor," Sens. Actuators B **153**, 392–397 (2011).
5. S. Kim, J. Choi, M. Jung, S. Joo, and S. Kim, "Silicon carbide-based hydrogen gas sensors for high-temperature applications," Sensors **13**, 13575–13583 (2013).
6. Y.-I. Chou, H.-C. Chiang, and C. C. Wang, "Study on Pd functionalization of microcantilever for hydrogen detection promotion," Sens. Actuators B **129**, 72–78 (2008).
7. S. Dong, F. Bai, J. Li, and D. Viehland, "Sound-resonance hydrogen sensor," Appl. Phys. Lett. **82**, 4590–4592 (2003).
8. S. F. Silva, L. Coelho, O. Frazao, J. L. Santos, and F. X. Malcata, "A review of palladium-based fiber-optic sensors for molecular hydrogen detection," IEEE Sens. J. **12**, 93–102 (2012).
9. R. Tabassum, S. K. Mishra, and B. D. Gupta, "Surface plasmon resonance based fiber optic hydrogen sulphide gas sensor utilizing Cu/ZnO thin films," Phys. Chem. Chem. Phys. **15**, 11868–11874 (2013).
10. X. Bévenot, A. Trouillet, C. Veillas, H. Gagnaire, and M. Clément, "Surface plasmon resonance hydrogen sensor using an optical fibre," Meas. Sci. Technol. **13**, 118–124 (2002).
11. V. P. Minkovich, D. Monzon-Hernondez, J. Villatoro, and G. Badenes, "Microstructured optical fiber coated with thin films for gas and chemical sensing," Opt. Express **14**, 8413–8418 (2006).
12. Z. Yu, L. Jin, L. Chen, J. Li, Y. Ran, and B.-O. Guan, "Microfiber Bragg grating hydrogen sensors," IEEE Photon. Technol. Lett. **27**, 2575–2578 (2015).
13. X. Wei, T. Wei, H. Xiao, and Y. S. Lin, "Nano-structured Pd-long period fiber gratings integrated optical sensor for hydrogen detection," Sens. Actuators B **134**, 687–693 (2008).
14. N. Basumallick, P. Biswas, R. M. Carter, R. R. J. Maier, S. Bandyopadhyay, K. Dasgupta, and S. Bandyopadhyay, "Design of palladium-coated long-period fiber grating for hydrogen sensing," J. Lightwave Technol. **34**, 4912–4919 (2016).
15. M. Yang and J. Dai, "Fiber optic hydrogen sensors: a review," Photon. Sens. **4**, 300–324 (2014).
16. M. Eryurek, Y. Karadag, N. Tasaltin, N. Kilinc, and A. Kiraz, "Optical sensor for hydrogen gas based on a palladium-coated polymer microresonator," Sens. Actuators B **212**, 78–83 (2015).
17. N. A. Yebo, D. Taillaert, J. Roels, D. Lahem, M. Debliquy, D. V. Thourhout, and R. Baets, "Silicon-on-insulator (SOI) ring resonator-based integrated optical hydrogen sensor," IEEE Photon. Technol. Lett. **21**, 960–962 (2009).
18. L. F. Aval and S. M. Elahi, "Hydrogen gas detection using MOS capacitor sensor based on palladium nanoparticles-gate," Electron. Mater. Lett. **13**, 77–85 (2017).
19. L. Coelho, J. Almeida, J. Santos, and D. Viegas, "Fiber optic hydrogen sensor based on an etched Bragg grating coated with palladium," Appl. Opt. **54**, 10342–10348 (2015).
20. O. Cernohorsky, K. Zdansky, J. Zavadil, and P. Kacerovsky, "Palladium nanoparticles on InP for hydrogen detection," Nanoscale Res. Lett. **6**, 410–414 (2011).
21. L. Zhou, X. Sun, X. Li, and J. Chen, "Miniature microring resonator sensor based on a hybrid plasmonic waveguide," Sensors **11**, 6856–6867 (2011).
22. A. Daraei and M. E. Daraei, "Thin cylindrical slot in an optical microdisk cavity for sensing biomaterials," Appl. Phys. A **123**, 216 (2017).
23. X. Sun, D. Dai, L. Thylén, and L. Wosinski, "Double-slot hybrid plasmonic ring resonator used for optical sensors and modulators," Photonics **2**, 1116–1130 (2015).
24. A. D. Rakic, A. B. Djurisic, J. M. Elazar, and M. L. Majewskii, "Optical properties of metallic films for vertical-cavity optoelectronic devices," Appl. Opt. **37**, 5271–5283 (1998).
25. J. Zou, M. Balberg, C. Byrne, C. Liu, and D. J. Brady, "Optical properties of surface micromachined mirrors with etch holes," J. Microelectromech. Syst. **8**, 506–513 (1999).
26. M. Gabalis, D. Urbonas, and R. Petruskevicius, "A perforated microring resonator for optical sensing applications," J. Opt. **16**, 105003 (2014).
27. D. Duchesne, P. Cheben, R. Morandotti, B. Lamontagne, D.-X. Xu, S. Janz, and D. Christodoulides, "Group-index birefringence and loss measurements in silicon-on-insulator photonic wire waveguides," Opt. Eng. **10**, 104602 (2007).
28. B. D. Adams and A. Chen, "The role of palladium in a hydrogen economy," Mater. Today **14**(6), 282–289 (2011).

29. J.-S. Noh, J. M. Lee, and W. Lee, “Low-dimensional palladium nanostructures for fast and reliable hydrogen gas detection,” Sensors **11**, 825–851 (2011).
30. L. Goddard, Y. W. Kai, A. Garg, E. Behymer, G. Cole, and T. Bond, “Measurements of the complex refractive index of Pd and Pt films in air and upon adsorption of H_2 gas,” in *21st Annual Meeting of the IEEE Lasers and Electro-Optics Society, LEOS* (2008).
31. B. G. Griffin, A. Arbabi, A. M. Kasten, K. D. Choquette, and L. L. Goddard, “Hydrogen detection using a functionalized photonic crystal vertical cavity laser,” IEEE J. Quantum Electron. **48**, 160–168 (2012).